ACS APPLIED MATERIALS & INTERFACES

Research Article

www.acsami.org

Porous Fluorine-Doped γ-Fe_2O_3 Hollow Spheres: Synthesis, Growth Mechanism, and Their Application in Photocatalysis

Lu-Ping Zhu,*[,†] Ling-Ling Wang,[†] Nai-Ci Bing,[†] Chao Huang,[†] Li-Jun Wang,*[,†] and Gui-Hong Liao[‡]

[†]School of Urban Development and Environmental Engineering, Shanghai Second Polytechnic University, Shanghai 201209, China

[‡]Technical Institute of Physics and Chemistry, Chinese Academy of Sciences, Beijing 100190, China

Supporting Information

ABSTRACT: Porous fluorine-doped maghemite(γ-Fe_2O_3) hollow spheres have been prepared by facile route based on solvothermal reaction and sequential calcinations. The composition and morphology of the as-prepared samples were characterized by various techniques. The SEM and TEM results showed that the as-synthesized products exhibited a spherical morphology with porous hollow structures. Ultraviolet−visible (UV−vis) diffuse reflectance spectra display that the optical performance of γ-Fe_2O_3 products are related to their structure and the fluorine concentrations. The porous hollow structured fluorine-doped γ-Fe_2O_3 spheres exhibit ferromagnetic properties with relatively high saturation magnetization at room temperature. According to the experimental results, a formation mechanism of the fluorine-doped γ-Fe_2O_3 hollow spheres has been presented. Under UV light irradiation, the photocatalytic degradation activities of the as-synthesized fluorine-doped γ-Fe_2O_3 samples for RhB dye were 2−5 times higher than that of the undoped sample. The prepared fluorine-doped γ-Fe_2O_3 hollow spheres will also aroused great interest for their application in catalysis, separation technology, sensors, nanotechnology, and biomedical fields

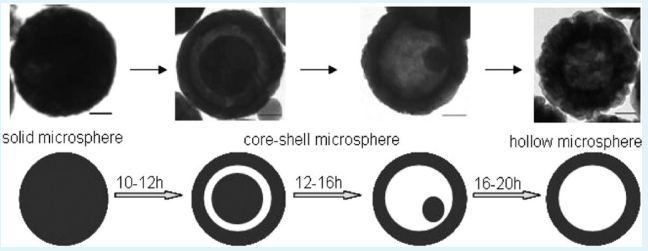

KEYWORDS: *fluorine-doped γ-Fe_2O_3, hollow spheres, synthesis, growth mechanism, optical properties, photocatalysis*

INTRODUCTION

Semiconductor photocatalysis, which is an efficient method to convert photon energy into chemical energy and decompose pollutants in air and water, has attracted great research interest. The process is based upon the fact that the photogenerated charges can be trapped on the surface of photocatalysts, which can result in interfacial electron-transfer reactions with various substrates.[1−4] Since the first report on photoelectrochemical splitting of water over n-TiO_2 electrodes,[5] TiO_2 has been considered as the most promising photocatalytic material, and is widely used in the field of the environment. However, a major deficiency of semiconductor photocatalytic materials is the need of an additional separation process to realize the separation of catalyst from the treated water. To overcome this disadvantage, researchers have developed magnetic photocatalysts to enable the easy recovery of the catalyst under the external magnetic field.[6−9] So far, the developed magnetic photocatalytic materials is mostly used magnetite (Fe_3O_4) or maghemite (γ-Fe_2O_3)[6,7] or spinel-like ferrites ($NiFe_2O_4$, $Zn_{0.35}Ni_{0.65}Fe_2O_4$)[8,9] as the magnetic cores. However, the direct contact between TiO_2 and magnetic cores may the Fe_3O_4 or γ-Fe_2O_3 act as recombination centers of photogenerated electrons and holes, which leads to the low photocatalytic efficiency. To improve the photoactivity of the magnetic photocatalytic systems, we can implant the insulator, which is chemically inert and electronically passive toward titanium oxide, to reduce the recombination of electrons and holes. It has been reported that the use of a SiO_2 layer between the Fe_3O_4 or γ-Fe_2O_3 core and the TiO_2 shell can enhance the photoactivity of the photocatalytic materials by blocking the injection of charges from TiO_2 particles to magnetic particles.[7] Similarly, the $TiO_2/SiO_2/NiFe_2O_4$ and $TiO_2/SiO_2/Zn_{0.35}Ni_{0.65}Fe_2O_4$ photocatalysts display promoted photocatalytic activity for degradation of organic species.[8,9] Even so, compared with that of the pure TiO_2, the photoactivity of the composite photocatalyst was considerably lower owing to the coating of SiO_2 around the surface of magnetic cores. In addition, the preparation of the composite system generally requires considerably multifarious process, hence limiting their applications. No doubt, there are three important factors to determine the application of magnetic photocatalyst, i.e., the magnetic properties, the stability, and the photoactivity of all photocatalysts. Therefore, the search for facile, mild, and easily controlled methods to prepare magnetic materials with high photocatalytic activity, good stability, and magnetic property is of great significance. To date, various magnetic nanostructured materials of γ-Fe_2O_3 and Fe_3O_4, such as nanorods,[10] nanotubes,[11] solid or hollow microspheres,[12,13] and flowerlike nanostructures,[14] have been prepared by various synthetic techniques. γ-Fe_2O_3, a very attractive semiconductor magnetic materials, has been applied extensively to magnetic storage

Received: September 3, 2013
Accepted: November 18, 2013
Published: November 18, 2013

media, catalytic, biomedical, and other fields because of its good biocompatibility, high chemical stability, and excellent magnetic properties. Recently, it has been found that γ-Fe_2O_3 can be used as photocatalysts and showed same photocatalytic activity as α-Fe_2O_3.[15] However, compared with TiO_2 (E_g = 3.2 eV), the photocatalytic activity of Fe_2O_3 (E_g = 2.0 eV) is not high enough to meet the needs of practical application. Thus, how to to enhance the photoctivity of Fe_2O_3 is still a principal challenge. In order to improve physical and chemical properties of the semiconductor, numerous studies have been carried out in recent years. For example, the electronic properties of a TiO_2 photocatalyst can be modified by implantation of V and Cr.[16,17] ZnO-based dilute magnetic semiconductors(DMSs) can be realized by doping with Fe, Co, Ni.[18] Moreover, doping of ZnO with Co can adjust enrich surface states and energy band structure in both VL and UV regions.[19] As a result, novel photoluminescence (PL) properties of the ZnO nanoparticles were present.[19] In addition, Asahi and co-workers synthesized N-doped TiO_2 with a narrow band gap by sputtering TiO_2 target in a N_2−Ar gas mixture and sequential calcinations in N_2 gas.[20] Khan et al. reported that the band gap of n-TiO_2 can be decreased to 2.32 eV by annealing Ti metal in a natural gas flame.[21] Recently, high photocatalytic activity for decomposition of organic pollutants was obtained by doping and surface modification of TiO_2 with fluoride anions.[22,23] The photocatalytic activity of fluorine-doped $SrTiO_3$ was 2 times higher than that of the pure $SrTiO_3$.[24] The main reasons are due to the increase in effective electron mobility and the formation of oxygen vacancies. Therefore, the band gap and photocatalytic activity of γ-Fe_2O_3 nanoparticles can be modified and enhanced by doping of other elements. In addition, as we all know, the shape, size, and dimensionality of the materials has an important influence on their performances. It is found that the size, dimensionality, and morphology of photocatalyst are crucial parameters determining the photocatalytic properties. For instance, Yu et al. reported that the cagelike hollow superstructure can promote the photocatalytic activity of α-Fe_2O_3, which attributed the multiple reflections of light within the hollow spherical structures that facilitates more effective use of the light source.[25] Inspired by previous works,[16−27] we attempted to synthesize porous fluorine-doped γ-Fe_2O_3 hollow nanostructures using the aqueous synthesis method. So far, there are no reports on the synthesis, formation mechanism, and photocatalytic activity of fluorine-doped γ-Fe_2O_3 hollow spherical nanostructures. In this work, fluorine interstitially doped γ-Fe_2O_3 samples with different fluorine concentrations were fabricated by a solvothermal process followed by annealing in air.

The as-obtained samples are characterized by various techniques. A possible formation process about the hollow spherical structures has been presented accoding to the experimental results. Their photocatalytic activities were also discussed carefully, which exhibited an enhanced photocatalytic activity. These porous fluorine-doped γ-Fe_2O_3 hollow spherical nanostructures will find potential applications in sensing, catalysis, sensing, separation technology, nanotechnology, and biomedical fields.

EXPERIMENTAL SECTION

Synthesis. First, 30 mL solution composed of iron(III) chloride was obtained by dissolving Iron(III) chloride hexahydrate ($FeCl_3{\cdot}6H_2O$) in ethylene glycol (EG). Then, the required amounts of NH_4F were added to the above solution under vigorous stirring. In what follows, the value of R_F is used to describe the atomic ratio of F to Fe; these were 0, 0.1, 0.2, 0.4, 0.8, and 1.0 nominal atomic ratio in the synthesis solution. Subsequently, a certain amount of ethylenediamine (EDA) was added the above the mixture followed by stirring for an additional 3 h at ambient temperature to form a well-distributed brown emulsion, which was then transferred into a stainless-steel autoclave with an inner Teflon lining. The autoclave was sealed and maintained at 200 °C for 20 h. After solvothermal reaction, the autoclave was cooled naturally to room temperature. The resulting sediments were washed with distilled water and ethanol thoroughly, before it was dried in a vacuum oven at 60 °C for 8 h. The dried sediments were then calcined in air at 250 °C for 5 h.

Characterization. The phase and composition of the as-synthesized samples was recorded by X-ray powder diffraction (XRD) with a Rigaku D/max diffraction system, using a Cu−Kα radiation source (λ=1.5406 Å). The X-ray photoelectron spectroscopy (XPS) analysis were performed on an Axis Ultra DLD instrument from Kratos(UK) using an Al Kα X-ray radiation source at a power of 300 W. A Hitachi S-4800 scanning electron microscope (Japan) was used for scanning electron microscopy (SEM) and and X-ray energy-dispersive spectroscopy (EDS) analysis. The morphologies and structures of the as-synthesized samples were further examined using a transmission electron microscope (TEM, Hitachi-600 V). UV-vis diffuse reflectance spectra of the as-obtained samples were recorded by using a UV-vis spectrophotometer (Shimadzu 2550). A vibrating sample magnetometer (VSM, Lakeshore 7307, USA) was used to measure the magnetic properties of the as-synthesized samples at room temperature. Nitrogen adsorption-desorption data were collected by using a Micromeritics (NOVA 4200e) analyzer at 77.35 K after heating the sample at 100 °C for 2 h. The surface areas of the synthesized samples were estimated using the Brunauer−Emmett−Teller (BET) method from the linear part of the BET plot (P/P_0 = 0.05-0.3).

Measurement of Photocatalytic Activity. The photocatalytic degradation of Rhodamine-B (RhB) was selected to evaluate the photocatalytic activity of the fluorine-doped γ-Fe_2O_3 hollow spheres under ultraviolet light irradiation (100 W high-pressure mercury lamp with a main emission wavelength of 365 nm). In a typical photocatalytic experiment, 20 mg of the as-synthesized samples was dispersed into 200 mL RhB solution (10 mg/L). The adsorption-desorption equilibrium between the RhB and the photocatalyst was gained after the suspensions were stirred for 30 min in the dark. The suspension was then exposed to ultraviolet (UV) light irradiation under continuous stirring. During irradiation, ~3 mL of the suspension continually was sampled and centrifuged to remove the photocatalyst particles at certain time intervals. The concentrations of the RhB were monitored on a UV−vis spectrophotometer (Shimadzu 2550) by measuring the absorbance at 553 nm during the photodegradation process.

RESULTS AND DISCUSSION

Morphology and Structure. The crystallographic structure and composition of the sample were identified by XRD and XPS. Figure 1 shows the XRD patterns of as-synthesized γ-Fe_2O_3 samples with different fluorine concentrations. All of the prepared fluorine-doped γ-Fe_2O_3 powders displayed a good crystallinity. These sample powders gave rise to well-established peaks, which can be ascribed to the (101), (103), (004), (112), (200), (105), (211) planes of γ-Fe_2O_3. The XRD investigation indicates that the crystallographic phase of all the prepared fluorine-doped γ-Fe_2O_3 powders belongs to spinel structured γ-Fe_2O_3 (JCPDS card No. 39-1346). Moreover, it is important to note that F doping did not result in significant changes in peak position of the prepared samples. This should be attributed to the fact that the ionic radius of doped F (0.133 nm) atom is almost similar to that of the replaced oxygen atom (0.132 nm). In addition, with increasing R_F, the peak intensities of γ-Fe_2O_3 gradually increase and the widths of peaks become narrower, consistent with increases in average crystal size and crystallinity. This is consistent with the previous report that fluoride enhances

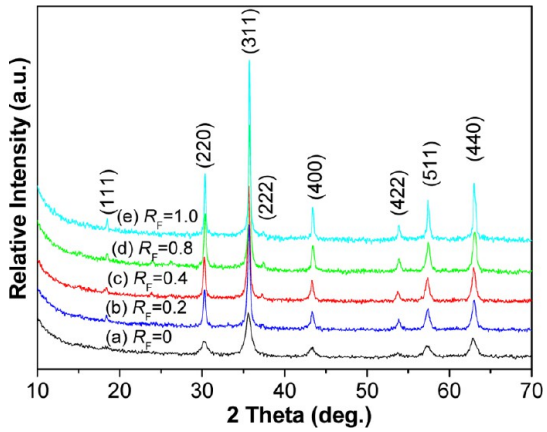

Figure 1. XRD patterns of the samples with different R_F values: (a) 0, (b) 0.2, (c) 0.4, (d) 0.8, (e) 1.0.

the crystallization of materials and promotes the growth of crystallites.[28]

Figure 2a shows XPS survey spectra of the as-obtained γ-Fe_2O_3 sample with R_F = 0, R_F = 1.0. The well-established photoelectron peaks appeared at ~711, ~725, and ~531 eV can be ascribed to the Fe $2p_{3/2}$, Fe $2p_{1/2}$, and O 1s in both cases. A C 1s signal peak at 285 eV should comes from the XPS instrument itself. In addition, an additional sharp peak at ~686 eV, as expected, is observed in the survery of the as-obtained γ-Fe_2O_3 sample with R_F = 1.0, which can attribute to the F 1s. The high-resolution XPS regional spectra of the main constituents Fe 2p, F 1s and O 1s of the γ-Fe_2O_3 samples were recorded for a more detailed analysis (Figure 2b–d). For pure γ-Fe_2O_3 samples, the binding energy (BE) of Fe $2p_{3/2}$ is equal to 711.2 eV and that of Fe $2p_{1/2}$ is equal to 724.8 eV, with a split of 13.6 eV between the two peaks (Figure 2b), which is identical to the reported results.[29] The BE of fluorinated γ-Fe_2O_3 samples was lower than that of pure γ-Fe_2O_3 samples, suggesting that the local chemical state was influenced by doping with F. An XPS spectrum of the F 1s of fluorine-doped γ-Fe_2O_3 powders was showed in Figure 2(c). Usually, the BE of 684 eV is corresponding to the F ions adsorbed on the samples, and that of 688 eV corresponds to the F ions in the lattice.[30] So, the peak at ~686 eV (F 1s) may be composed of two contributions, which is in consistent with the previous report.[32] One contribution is due to physical adsorption of F ions in γ-Fe_2O_3 surface. Another contribution is attributed to the F in the Fe-based solid solution, which may be achieved by replacing the oxygen of Fe_2O_3 lattice. This process can occur easily because of the ionic radius of F (0.133 nm) is virtually identical to that of O (0.132 nm) in the lattice of Fe_2O_3. When F^- ions replace O^{2-}, a charge imbalance is generated. The charge imbalance can slow the recombination of the electron-hole pairs, providing photogenerated holes with more opportunities to combine with the adsorbed H_2O. Therefore, more reactive oxygen species such as hydroxyl radicals (·OH) will be created. These oxygen species, having strong oxidative abilities, are playing a fundamental role in the photodegradation of organics. The XPS spectra of the O 1s region of γ-Fe_2O_3 samples are shown in Figure 2d. The O 1s spectrum of the pure γ-Fe_2O_3 samples was symmetric. The main peak of O 1s appeared at about 530.2 eV, which is corresponding to lattice oxygen of Fe_2O_3. For the fluorine-doped γ-Fe_2O_3 sample, an asymmetric region can be observed in the O 1s spectrum. Besides a main peak of O 1s appeared at about 529.9 eV, two shoulder peaks at higher binding energy could be identified, which also indicated that the local chemical state was influenced by doping with F.

The morphologies, structures, and sizes of the as-synthesized fluorine-doped γ-Fe_2O_3 sample were elucidated by SEM and

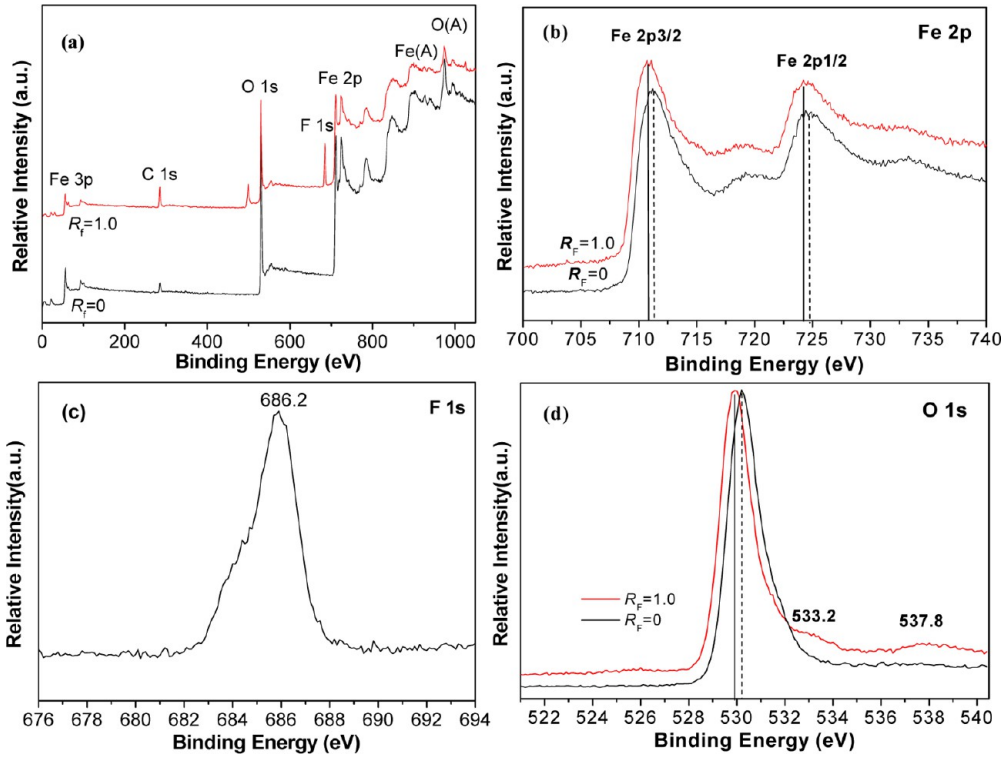

Figure 2. (a) XPS survey spectra of γ-Fe_2O_3 samples prepared at R_F = 0 and R_F = 1.0. (b–d) High-resolution XPS spectra of Fe 2p, F 1s, and O 1s of corresponding fluorinated γ-Fe_2O_3 samples.

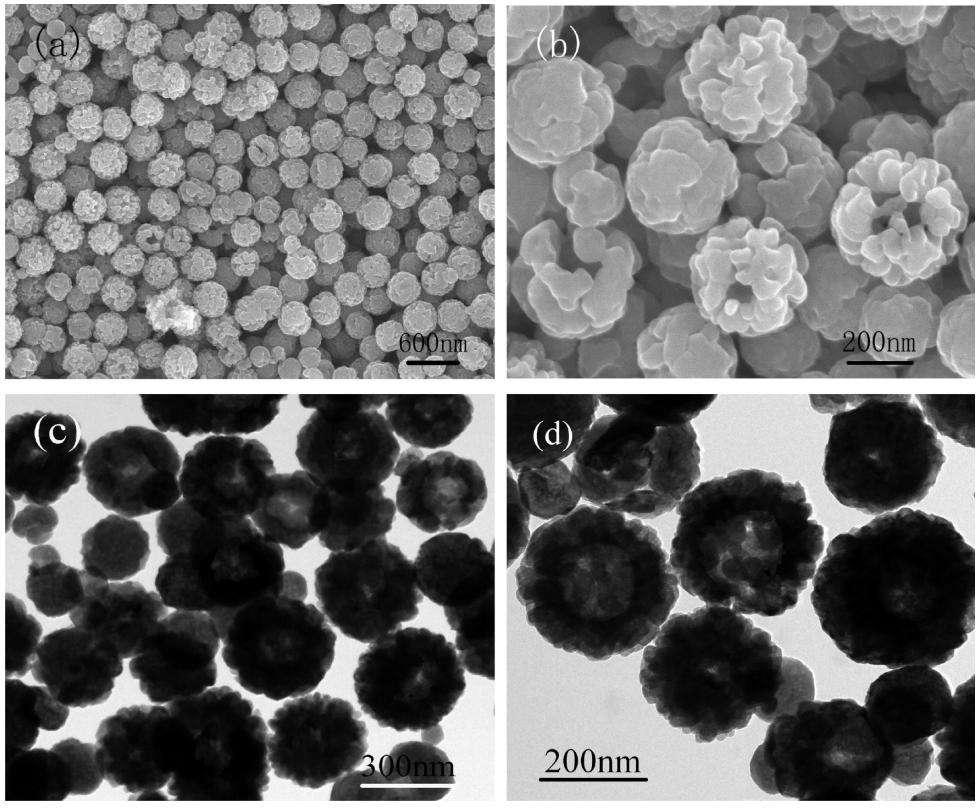

Figure 3. SEM images of the product obtained at R_F = 1.0: (a) low magnification, (b) high magnification. TEM images: (c) low magnification, (d) high magnification.

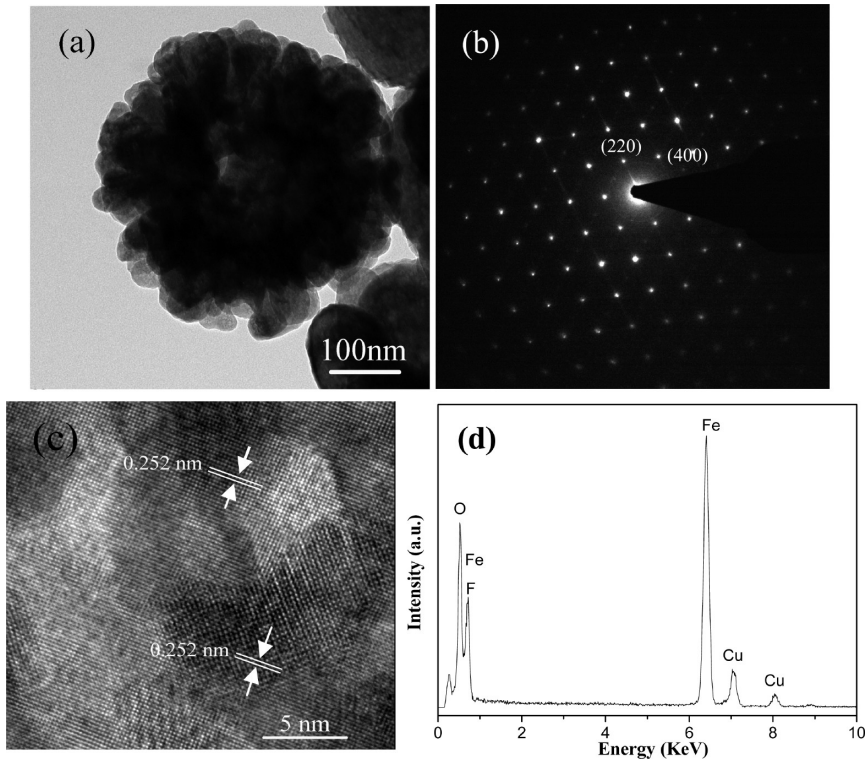

Figure 4. (a) TEM image of single sphere obtained at R_F = 1.0. (b) Corresponding SAED pattern, (c) HRTEM image, (d) energy-dispersive X-ray spectrum (EDS) of the as-prepared samples.

TEM. The low magnification SEM images (Figure 3a, b) show that the as-synthesized samples consist of a wealth of uniform spheres. Figure 3b showed the high-magnification SEM image of the as-synthesized samples. It can be clearly observed that the

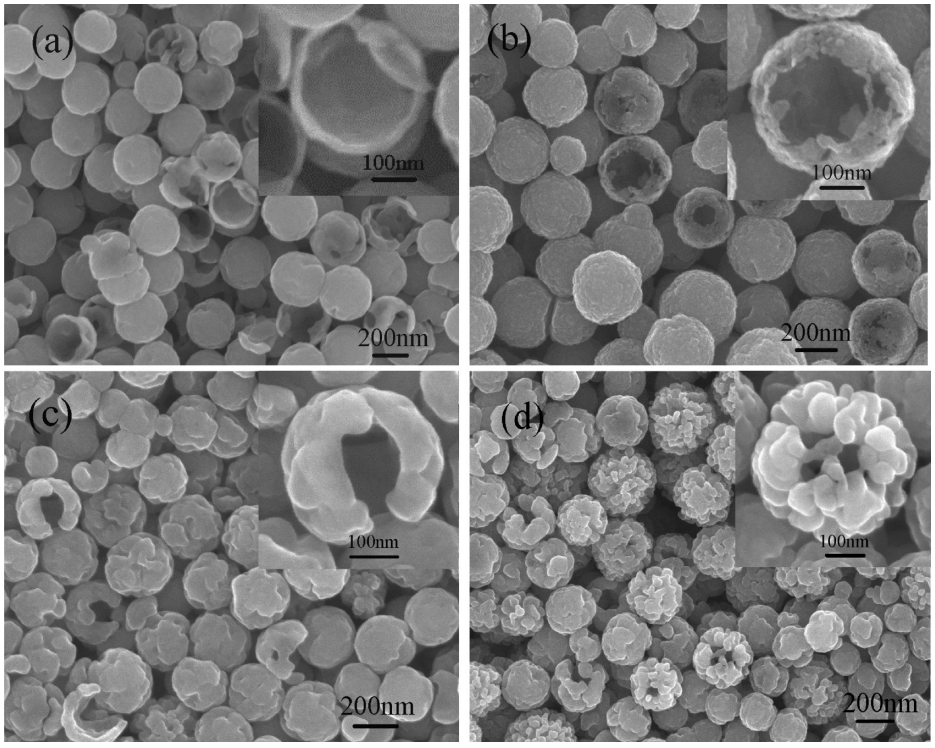

Figure 5. SEM images of γ-Fe_2O_3 samples prepared with varying R_F : (a) R_F = 0, (b) R_F = 0.4, (c) R_F = 0.8, and (d) R_F = 1.0. The insets show the corresponding high-magnification SEM images of the as-synthesized products.

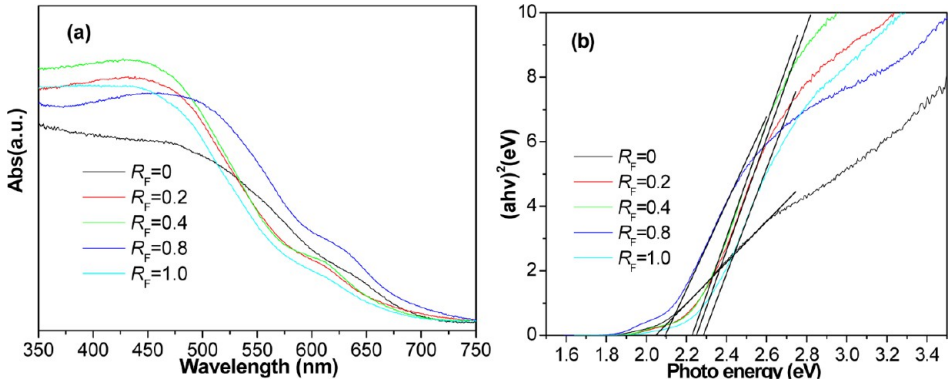

Figure 6. (a) UV−vis diffuse reflectance spectra and (b) plots of $(\alpha h\nu)^2$ versus photon energy $h\nu$ of the γ-Fe_2O_3 samples with different R_F values.

surfaces of the spheres are not clearly smooth and have a great number of cracks. This result indicated that the spheres have a porous structure. Images c and d in Figure 3 showed the low- and high-magnification TEM images of the as-synthesized samples, from which a strong contrast between the pale center region and a dark edge can be observed, indicating the spheres have hollow structure. The mean size of the hollow spheres is about 250 nm, while the thickness of the shell is about 40 nm. From the single hollow sphere (Figure 4a), it can be clearly seen that the hollow spherical structure is highly porous, and is composed of irregular shaped nanocrystal clusters with the size of approximately 20 nm (consistent with the calculation value). The above SEM and TEM results together conform that the as-obtained samples have uniform porous hollow spherical structures. In addition, it should be mentioned that the well-dispersed porous hollow spheres are narrow size distribution and the morphological yield nearly reaches to 100%. The corresponding SAED pattern(Figure 4b) of an individual sphere shows regular and well-defined electron diffraction spot array, indicating that the as-synthesized sample is single crystalline in nature and has a cubic spinel structure with phase purity. The high-resolution TEM (HRTEM) image providing the clear lattice fringe, as shown in Figure 4c, also confirms that the as-obtained hollow spheres are high crystallinity and single crystalline, in agreement with the SAED analysis. The lattice spacing is measured to be 0.252 nm based on the HRTEM image, which corresponds well with the (311) plane of cubic γ-Fe_2O_3. The EDS result (Figure 4d) indicates that the as-prepared samples are mainly composed of Fe, O, and F elements. The atomic ratio of Fe/O/F is 2:3.3:0.1, which is not in good accordance with the nominal atomic ratio of γ-Fe_2O_3. The Cu signal comes from the copper grid.

Figure 5 shows typical SEM micrographs of the γ-Fe_2O_3 samples prepared with varying R_F values. In the absence of fluoride, the as-obtained samples are hollow spheres (Figure 5a), which is the same as the reported.[31] The average diameter and wall thickness of hollow spheres are about 250 and 20 nm,

respectively. At R_F = 0.4, partially broken spheres also display hollow interiors (see Figure 5b). Comparing with the sample obtained at R_F = 0, as shown in Figure 5a, the external surface is rougher and the shell thickness is thicker (Figure 5b, inset). It is well known from the synthesis of particles that the dopant atoms greatly affect the structure, size, and morphology of the resulting particles. Increasing R_F to 0.8 also produces hollow spheres (see Figure 5c), although the external surface is rougher and the shell thickness is more thicker (Figure 5c, inset). When the fluoride concentration increases to R_F = 1, the integrated and regular hollow spheres almost disappear and hollow hierarchitectures assembled with nanocrystal clusters form (Figure 5d). The XRD results and the above observations imply that high fluoride: ferrum molar ratios favor crystallization of maghemite over hollow sphere formation via Ostwald ripening.[32]

Optical Properties, Nitrogen Sorption, and Magnetic Properties. The optical performance of the fluorine-doped γ-Fe_2O_3 samples were carried out by using UV−vis spectrophotometer. Figure 6a shows the UV−vis spectra of the γ-Fe_2O_3 samples with different fluorine concentrations. The spectra of all fluorine-doped γ-Fe_2O_3 products show that the photoabsorption has an obvious increase at wavelengths lower than about 750 nm. The absorption edge of the fluorine-doped γ-Fe_2O_3 samples displays an appreciable blue-shift. The band gap energy E_g of a semiconductor can be more accurate calculated by using the following equation

$$(\alpha h\nu)^n = B(h\nu - E_g) \quad (1)$$

where α, h, ν, B, and E_g are the absorption coefficient, Planck constant, light frequency, a constant, and band gap, respectively.[33] Thereinto, n depends on the characteristics of the transition in a semiconductor, which is either 2 for direct inter-band transition or 1/2 for indirect inter-band transition.[33] For γ-Fe_2O_3, the value of n is 2 for the direct transition. Figure 6b shows the $(\alpha h\nu)^2$ vs photon energy $h\nu$ curve for the as-obtained samples with different fluorine concentrations. The E_g values of as-synthesized γ-Fe_2O_3 samples prepared at R_F = 0, 0.2, 0.4, 0.8, and 1.0 are estimated to be 2.04, 2.25, 2.23, 2.09, and 2.29 eV from the $(\alpha h\nu)^2 - h\nu$ plots, respectively. Known to us all, the band gap energy of semiconductor nanoparticles strongly depend on their sizes and structures. In this study, although the samples with different amounts of fluorine present almost the same sizes, the samples show an appreciable blue shift in the band gap transition (from 2.04 to 2.29 eV) when the R_F value increases from 0 to 1.0. Obviously, the F doping has a great influence on the shape, structure, optical property, and the band gap. Recent studies on such doping have provided considerable insight to the electronic structure and properties of the host oxides.[34] To fully understand the experimental results, further work is underway to find out the effect of fluorine doping on the electronic structure of the as-synthesized γ-Fe_2O_3 samples.

The magnetic performance of the as-synthesized fluorine-doped γ-Fe_2O_3 samples were investigated by VSM at room temperature. The hysteresis loops of the as-synthesized fluorine-doped γ-Fe_2O_3 samples are exhibited in Figure S1 (see the Supporting Information). It can be seen from Figure S1 in the Supporting Information that the saturation magnetizations (M_s) are 69.73, 66.70, 66.03, and 61.99 emu/g, remanent magnetization (M_r) are 8.81, 8.37, 3.25, and 6.90 emu/g, coercivity (H_c) are 73.10, 72.80, 49.2, and 67.8 Oe for fluorine-doped γ-Fe_2O_3 samples with R_F= 0, 0.2, 0.4, 1.0, respectively. As expected, the saturation magnetization for fluorine-doped γ-Fe_2O_3 hollow spheres are also lower than for the corresponding solid spheres (M_s = 81 emu/g)[12] and bulk γ-Fe_2O_3 (74 emu/g).[35] As we know, the magnetic performances of the product strongly depend on the size, structure and shape. The different magnetic properties of as-obtained samples may ascribe the fact that the as-synthesized γ-Fe_2O_3 samples have different fluorine concentrations, morphologies, and structures. In spite of this, their maximum saturation magnetization, 66.70, 66.03, and 61.99 emu/g (see Figure S1b−d), respectively, are enough strong to preserve their good performance of magnetic recovery.[36]

The specific surface areas and pore size distribution of the as-synthesized samples with varying R_F values were estimated by measuring the nitrogen adsorption−desorption isotherms, as shown in Figure S2 (see the Supporting Information). The isotherms of the as-obtained samples be classified as type IV with a distinct hysteresis loop (at 0.5−1.0 p/p_0), which suggests that all the samples possess a mesoporous structure (2−50 nm in size).[37] Furthermore, the obtained hysteresis loop was shifted to a relatively higher pressure when $P/P_0 \approx 1$, indicating the presence of macropores (>50 nm).[37] The above results were further confirmed by the corresponding pore-size distributions calculated from the nitrogen isotherm by the Barrett−Joyner−Halenda (BJH) method, in which mesopores (10.0−25.0 nm) and macropores with a maximum pore diameter of ca. 100 nm can be found (inset in Figure S2 in the Supporting Information). The smaller pores may arise from the crystal growth process, whereas the larger pores can be ascribed to the space between the stacked γ-Fe_2O_3 nanocrystal clusters and the hollow structure. In addition, the peaks of pore size of the samples shift to the right after the sample is doped with fluorine, showing an increase in average pore size. It means that the crystallinity of as-synthesized γ-Fe_2O_3 is improved, which is well in agreement with the XRD analysis. The mean pore diameters and BET surface area of the as-obtained samples are listed in Table 1. In general, the as-synthesized samples display an obvious increase in the mean pore diameter and BET surface area with the increase of R_F. This result may be attributed to several factors, including increases in the rate of Ostwald ripening, growth of the γ-Fe_2O_3 nanocrystal clusters, and structure of the γ-Fe_2O_3 hollow spheres.

Table 1. Brunauer−Emmett−Teller (BET) Surface Area and Mean Pore Diameters of the As-Prepared Samples

sample	R_F	BET surface areas (m^2 g^{-1})	mean pore diameters (nm)
1	0	9.14	13.33
2	0.2	11.16	15.29
3	0.4	14.31	23.98
4	1.0	18.52	34.45

Mechanism for the Formation of Fluorine-Doped γ-Fe_2O_3 Hollow Spheres. To investigate the formation process of the hollow spheres and their growth mechanism in more detail, we conducted time-dependent experiments. Figure 7a shows the representative TEM images of the samples obtained at different time intervals. The TEM results revealed that the reaction time plays a very important role in the formation of the hollow spheres. For example, only solid spheres with a diameter of about 250 nm can be obtained when the reaction time was equal to 10 h. When the time was extended to 12 h, a core−shell hollow spherical structure confirmed by the obvious contrast between the dark edges/cores and the pale hollow part is obtained and their surface becomes rough. The mean diameter of the cores is about 150 nm. Further extending the reaction time to 16 h, the average diameter of the cores decreases to around 30

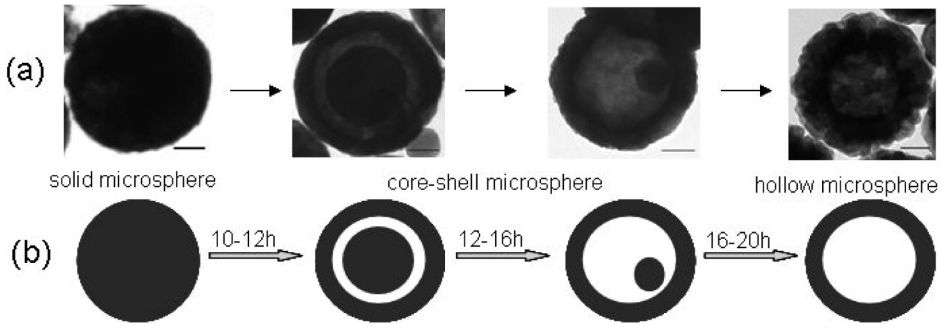

Figure 7. (a) TEM images of the solid sphere, core–shell sphere, and hollow sphere obtained at 200 °C after 10, 16, and 20 h, respectively. The scale bar represents 50 nm. (b) Schematic illustration of the formation of the hollow spheres.

nm, indicating that evacuation is still in progress. When the duration time was further extended to 20 h, a completely porous hollow sphere with larger crystallite size is acquired. According to the above experimental results, a possible formation process based on assembly-then-inside-out evacuation can be proposed, as illustrated in Figure 7b. Fe^{3+} reacts with EDA in EG solution to form a relatively stable complex ion of $[Fe(EDA)_3]^{3+}$ with octahedral structure, as described previously.[38] Afterward, the complex ion decomposed and released EDA under the solvothermal conditions. As a result, the FeOOH was first formed. Subsequently, the formed FeOOH nanoparticles can redissolve and reacted with the obtained Fe^{2+} at the presence of F^- to form fluorine-doped nanoparticles. The freshly crystalline nanoparticles are unstable and have a tendency to form larger congeries, which may be driven by the magnetic dipole–dipole interaction and the minimization of interfacial energy.[39] However, compared to the aqueous solution, the EG solution has fewer surface hydroxyls and greater viscosity, the nucleation and aggregation of the nanocrystals are kinetically slower in the EG solution, which lead to form perfectly oriented assemblies by the adequate rotation to find the low-energy configuration interface.[40] Afterward, the formed loose spherical assemblies became gradually compact solid spheres through further crystallization based on the Ostwald ripening mechanism. With the extension of reaction time, an interior hollow structure can be formed gradually based on the inside-out evacuation and Ostwald ripening mechanism. In the fabrication of Fe_3O_4, SnO_2, and ZnS hollow spherical structures, such a process was also observed.[31,41,42] The above mechanism can be well-supported by the time-dependent experiments. Apart from the fluorine concentrations, the amount of EDA also plays a significant role in the formation, structure, and morphology of the as-synthesized γ-Fe_2O_3 samples when the other synthetic parameters were not changed. It is same as our previous study on the preparation of magnetite hollow spherical structures by EDA-assisted self-assembly then inside-out evacuation strategy.[31] Generally speaking, a relatively low amount of EDA is not conducive to the formation of the hollow spheres, but is conducive to forming solid spherical structures. When the added EDA was 3.0 mL, hollow spheres with a core-shell structure were obtained, as exhibited in Figure S3 (see the Supporting Information), indicating that the given amount of EDA is not enough to complete the inside-out evacuation process at the the presence of F^- and the evacuation is still in progress. Similar to the hollow spheres, the core-shell hollow spheres also comprise primary nanoparticles. With the increase in the amount of EDA, the number of of hollow spheres increased markedly. However, once the EDA amount meets or exceed 5.0 mL, hollow spherical structures will not be obtained. The nanoparticles began to tend to assemble into large particles. For example, cauliflower-like congeries instead of hollow spheres can be obtained when the amount of EDA reached to 6.0 mL, which is consistent with our previous report.[43]

Photocatalytic Activity. The photoactivities of the as-obtained γ-Fe_2O_3 samples were investigated by the degradation of RhB dye in water under UV light irradiation (λ = 365 nm). On the basis of the results of refs 44 and 45, the photocatalytic degradation processes of the RhB were monitored by measuring the characteristic absorbance at 553 nm. The temporal evolution of the spectral changes during the photocatalytic degradation of RhB over γ-Fe_2O_3 with R_F = 0, R_F = 1.0 at the certain time intervals are shown in Figure 8. For γ-Fe_2O_3 with R_F = 1.0 used as photocatalyst, the maximum absorption at λ = 553 nm decreases

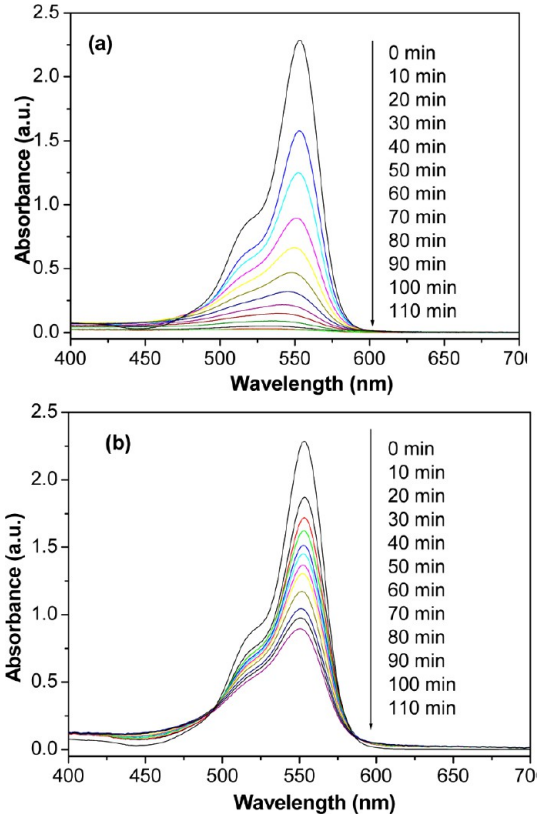

Figure 8. UV–vis absorption spectra during photocatalytic reaction of RhB over γ-Fe_2O_3 with different doped fluorine concentrations at different time intervals, (a) R_F = 0, (b) R_F = 1.

gradually with the increase in exposure and completely disappears after 110 min. (Figure 8(a)). No new absorption peaks can be observed in visible light and UV region, demonstrating that the photocatalytic degradation of RhB was completely during that reaction. In the case of γ-Fe_2O_3 catalyst with R_F = 0, the absorbance value (at λ = 553 nm) of RhB decreased from 2.287 to 0.881 after 110 min (Figure 8b). In addition, a significant shift of absorbance (at λ = 553 nm) is not observed during the photocatalytic process, as shown in panels a and b in Figure 8. This suggests that the fluorine doping does not change the photocatalytic degradation pathway of RhB in our system. The photocatalytic performances of the γ-Fe_2O_3 samples doped with different fluorine concentrations were studied by the degradation of RhB aqueous solution under UV irradiation (Figure 9a). The blank test shows that RhB can only be slightly

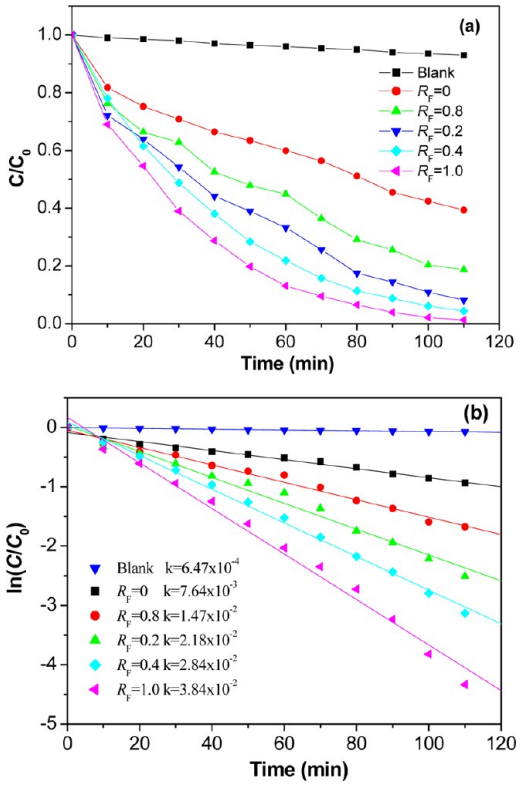

Figure 9. (a) Photocatalytic performances and (b) plots of $\ln(C/C_0)$ against time t of various samples: without catalyst, the fluorine-doped γ-Fe_2O_3 hollow spheres prepared with R_F = 0, 0.2, 0.4, 0.8, and 1.0, respectively. (C_0 = 10 mg/L, catalyst 0.02 g).

degraded under UV light irradiation without catalysts, which indicates that the direct adsorption and photolysis of catalysts plays a negligible role in the degradation of RhB. Interestingly, the completely different photodegradation rates of RhB can be obtained by the UV irradiation of the aqueous RhB/γ-Fe_2O_3 dispersions. The photodegradation rates of the as-synthesized fluorine-doped γ-Fe_2O_3 samples are much higher than that of pure γ-Fe_2O_3 samples. The enhanced photocatalytic efficiency of the as-synthesized fluorine-doped samples should be due to the fluorine doping. Furthermore, compared with that of the other fluorine-doped γ-Fe_2O_3, the sample of R_F = 1 exhibited the highest photocatalytic activity, although they have similar grain sizes. Figure 9b shows the determination of rate constant for RhB degradation over γ-Fe_2O_3 samples doped with different fluorine concentrations. The apparent rate constant of photodegradation of RhB can be determined by using the following expression[46]

$$\ln(C/C_0) = kt \quad (2)$$

where C_0 and C are the absorbance value (at λ = 553 nm) of RhB at t = 0 and t min time required for complete photodegradation, k is the apparent rate constant of the reaction, t is the irradiation time, respectively. The k was calculated from the slope of the $\ln(C/C_0)$ − t plots. It is indicated that the photocatalytic degradation of RhB over the as-synthesized γ-Fe_2O_3 hollow spheres with different fluorine concentrations roughly follows the pseudo-first-order reaction after 110 min of illumination. The sample of R_F = 0 shows a decent photocatalytic activity with a rate constant k of 7.64×10^{-3} min^{-1}. The photocatalytic activities of samples increase with an increase of doped fluorine concentration, except that the samples with R_F = 0.8. The k for RhB photocatalytic degradation over fluorine-doped γ-Fe_2O_3 prepared at R_F = 0.2, 0.4, 0.8, and 1.0 was determined to be 0.0218, 0.0284, 0.0147, and 0.0384 min^{-1}, respectively. It is obvious that fluorine-doped γ-Fe_2O_3 prepared at R_F = 1.0 displayed the highest photoactivity for the degradation of RhB. It is amazing that more than 90% of RhB has been degraded when the irradiation time reaches 110 min. Compared to the undoped sample, the k value for RhB photocatalytic degradation over fluorine-doped γ-Fe_2O_3 prepared at R_F = 1.0 raises 5.0 times.

Usually, in the photocatalytic reaction process, ·OH is thought to be one of the main reactive species that are responsible for the oxidation decomposition of the organic pollutants. Generally speaking, the formation rate of ·OH is larger, and the photocatalytic activity is higher. However, for Fe_2O_3 with a narrow band gap, ·OH can not be obtained during irradiation.[47] This could be ascribed to the band edge positions of Fe_2O_3 and the standard potential of $OH^-/{\cdot}OH$ and O_2/O_2^- couples.[47] Because of the photogenerated holes and electrons on Fe_2O_3 could not react with OH^-/H_2O and O_2 to form ·OH and O_2^-, respectively, therefore, no ·OH can be observed for Fe_2O_3.[47] So, the high photocatalytic activity may result from the appropriate fluorine concentrations, novel structure, and the relatively high BET surface area of 18.52 m^2/g, which is 2 times higher than that of the γ-Fe_2O_3 samples with R_F = 0.2 (from 11.16 to 18.52 m^2/g, as shown in Table 1.). This suggested that ·OH was not the only active species during the photocatalytic oxidation reaction process. Several research results also showed that reaction of photogenerated holes and organic compound can directly lead to the occurrence of photocatalytic oxidation.[42,48] Therefore, the formation rate of ·OH is not the unique factor to evaluate the photocatalytic activity of materials. The photocatalytic performances of these γ-Fe_2O_3 samples are strongly dependent on shape, structure, and fluorine concentrations.

As for the higher photoactivity of the as-obtained fluorine-doped γ-Fe_2O_3 samples, several reasons may be accounted. Firstly, the adsorption and desorption of the molecules on the surface of the catalyst had a strong influence on the catalytic process. The large specific surface area can result in a more unsaturated coordination sites to expose to the solution and help to promote the efficiency of the electron-hole separation.[49] Secondly, as is known to all that the photoactivities of semiconductor photocatalytic materials can be tuned by controlling the ratio of surface electron transfer rate to the electron-hole recombination rate. When the rate of surface electron transfer increase, the probabilities for recombination can be reduced and the photogenerated charge carriers can more easily transfer to the surface to degrade the absorbed RhB

molecules. Endo et al. reported that the effective mobility of electron would increase with the increasing of F^- content.[50] Therefore, when γ-Fe_2O_3 samples with fluorine doping, the photogenerated electrons could easily diffuse from the inner regions to the surface of the grains to present the redox function, which benefits the enhancement of the photocatalytic activity of γ-Fe_2O_3 samples. So, fluorine-doped γ-Fe_2O_3 samples exhibited higher photoactivity than that of undoped samples. Significantly, the higher photocatalytic activity of the hollow spheres prepared at R_F = 0.2, 0.4, 1.0 compared with those produced at R_F = 0.8, which may be ascribed to the larger band gaps of the formers. On the other hand, previous studies show that the porous structures with hollow internal cavity could not only increase the reaction chance and benefit to act with the organic compounds by the storage of more molecules, but also promote light-scattering inside the pores of the shell wall and within the interior cavity and allow the reactants and products to diffuse rapidly during the reaction.[51] It is speculated that pores and hollow internal cavity in the fluorine-doped γ-Fe_2O_3 hollow hierarchitectures contribute to the penetration of light waves as well as RhB solution deep into this catalyst, which greatly improves the photocatalytic properties of the photocatalyst.

Moreover, as its application, the stability of the catalyst is very important. In our case, all fluorine-doped γ-Fe_2O_3 samples also have stable photoactivity. The used samples can be regenerated by thorough washing with ethanol and deionized water following by drying in a vacuum oven at 60 °C for 3 h. The photocatalytic property for RhB catalytic degradation of the used fluorine-doped γ-Fe_2O_3 samples is almost invariable after three cycles. The typical SEM image of the samples used for three cycles was shown in Figure S4 (see the Supporting Information). The SEM result shown that the morphology and structure of the as-synthesized sample is almost no change, which is very significant for the stable photocatalytic activity of fluorine-doped γ-Fe_2O_3 hollow spheres.

CONCLUSIONS

In summary, we have developed a facile approach using a simple solvothermal process followed by calcinations for the controlled synthesis of porous hollow structured fluorine-doped γ-Fe_2O_3 spheres. Localized Ostwald-ripening and assembly-then-inside-out evacuation mechanism are the main driving forces for the formation of the porous hollow architectures. EDA plays a very important role in the formation of the porous fluorine-doped γ-Fe_2O_3 hollow spheres. NH_4F is employed as a dopant in the synthesis of fluorine-doped γ-Fe_2O_3 spheres, which strongly influences the morphology, crystallinity, structure, size, specific surface area, and photocatalytic performance of the γ-Fe_2O_3 samples. Compared to the undoped sample, the fluorine-doped γ-Fe_2O_3 samples exhibit a higher photocatalytic activity. We believe that the transfer of the photogenerated electrons and holes (instead of ·OH), larger band gaps, higher specific surface area, and porous hollow structure play significant roles in the excellent photocatalytic performance of fluorine-doped γ-Fe_2O_3 photocatalysts. In addition, these as-synthesized γ-Fe_2O_3 samples also exhibit ferromagnetic properties with relative high saturation magnetization at room temperature. The high photocatalytic activity, ferromagnetic properties, high specific surface area, and saturation magnetization will make them ideal candidates for applications in sensors, catalysis, separation technology, biomedical engineering, environmental engineering, and nanotechnology.

ASSOCIATED CONTENT

Supporting Information

Nitrogen adsorption−desorption isotherm and pore size distribution curve, TEM and SEM images, and room-temperature magnetization curves of the as-prepared samples. This material is available free of charge via the Internet at http://pubs.acs.org.

AUTHOR INFORMATION

Corresponding Authors

*E-mail: lpzhu@sspu.edu.cn. Tel/Fax: +86 21 50216301.
*E-mail: wang_lijun@yahoo.com.

Notes

The authors declare no competing financial interest.

ACKNOWLEDGMENTS

This work was supported by the National Natural Science Foundation of China (21101105 and 51174274), Shanghai Municipal Natural Science Foundation (10ZR1412200), and the Innovation Program of the Shanghai Municipal Education Commission (10YZ200). We are grateful to Prof. Shao-Yun Fu from Technical Institute of Physics and Chemistry (CAS) for helpful discussion and critical reading.

REFERENCES

(1) Sakthivel, S.; Kisch, H. *Angew. Chem., Int. Ed.* **2003**, *42*, 4908−4911.
(2) Fang, X.; Zhai, T.; Gautam, U. K.; Li, L.; Wu, L.; Bando, Y.; Golberg, D. *Prog. Mater. Sci.* **2011**, *56*, 175−287.
(3) Fang, X.; Bando, Y.; Gautam, U. K.; Ye, C. H.; Golberg, D. *J. Mater. Chem.* **2008**, *18*, 509−522.
(4) Alabi, T. R.; Yuan, D.; Bucknall, D.; Das, S. *ACS Appl. Mater. Interfaces* **2013**, *5*, 8932−8938.
(5) Fujishima, A.; Honda, K. *Nature* **1972**, *238*, 37−38.
(6) Beydoun, D.; Amal, R.; Low, G.; McEvoy, S. *J. Phys. Chem. B* **2000**, *104*, 4387−4396.
(7) Chen, F.; Xie, Y.; Zhao, J.; Lu, G. *Chemosphere* **2001**, *44*, 1159−1168.
(8) Chung, Y. S.; Park, S. B.; Kang, D. W. *Mater. Chem. Phys.* **2004**, *86*, 375−381.
(9) Shchukin, D. G.; Kulak, A. I.; Sviridov, D. V. *Photochem. Photobiol. Sci.* **2002**, *1*, 742−744.
(10) Lian, S.; Wang, E.; Kang, Z.; Bai, Y.; Gao, L.; Jiang, M.; Hu, C.; Xu, L. *Solid State Commun.* **2004**, *129*, 485−490.
(11) Liu, Z.; Zhang, D.; Han, S.; Li, C.; Lei, B.; Lu, W.; Fang, J.; Zhou, C. *J. Am. Chem. Soc.* **2005**, *127*, 6−7.
(12) Liu, X. M.; Fu, S. Y.; Xiao, H. M. *J. Solid State Chem.* **2006**, *179*, 1554−1558.
(13) Huang, Z.; Tang, F. *J. Colloid Interface Sci.* **2005**, *281*, 432−436.
(14) Zhong, L. S.; Hu, J. S.; Liang, H. P.; Cao, A. M.; Song, W. G.; Wan, L. J. *Adv. Mater.* **2006**, *18*, 2426−2431.
(15) Apte, S. K.; Naik, S. D.; Sonawane, R. S.; Kale, B. B. *J. Am. Ceram. Soc.* **2007**, *90*, 412−414.
(16) Anpo, M.; Takeuchi, M. *J. Catal.* **2003**, *216*, 505−516.
(17) Yamashita, H.; Harada, M.; Misaka, J.; Takeuchi, M.; Neppolian, B.; Anpo, M. *Catal. Today* **2003**, *84*, 191−196.
(18) Fert, A. *Thin Solid Films* **2008**, *517*, 2−5.
(19) Zhu, L. P.; Yang, Y.; Bing, N. *Chem. Lett.* **2011**, *40*, 390392−390394.
(20) Asahi, R.; Morikawa, T.; Ohwaki, T.; Aoki, K.; Taga, Y. *Science* **2001**, *293*, 269−271.
(21) Khan, S. U. M.; Al-Shahry, M.; Ingler, W. B. *Science* **2002**, *297*, 2243−2245.
(22) Yu, J. G.; Wang, W. G.; Cheng, B.; Su, B. L. *J. Phys. Chem. C* **2009**, *113*, 6743−6750.
(23) Lv, K.; Cheng, B.; Yu, J.; Liu, G. *Phys. Chem. Chem. Phys.* **2012**, *14*, 5349−5362.

(24) Huang, G.; Zhu, Y. *J. Phys. Chem. C* **2007**, *111*, 11952−11959.
(25) Yu, J.; Yu, X.; Huang, B.; Zhang, X.; Dai, Y. *Cryst. Growth. Des.* **2009**, *9*, 1474−1480.
(26) Cao, S. W.; Zhu, Y. J.; Ma, M. Y.; Li, L.; Zhang, L. *J. Phys. Chem. C* **2008**, *112*, 1851−1856.
(27) Zhu, L. P.; Wang, L. L.; Bing, N. C.; Jin, H. Y.; Liao, G. H.; Wang, L. J. *Mater. Lett.* **2012**, *88*, 164−167.
(28) Li, J.; Zeng, H. C. *J. Am. Chem. Soc.* **2007**, *129*, 15839−15847.
(29) Hyeon, T.; Lee, S. S.; Park, J.; Chung, Y.; Na, H. B. *J. Am. Chem. Soc.* **2001**, *123*, 12798−12801.
(30) Park, H.; Choi, W. *J. Phys. Chem. B* **2004**, *108*, 4086−4093.
(31) Zhu, L. P.; Xiao, H. M.; Zhang, W. D.; Yang, G.; Fu, S. Y. *Cryst. Growth. Des.* **2008**, *8*, 957−963.
(32) Yu, J. G.; Guo, H. T.; Davis, S. A.; Mann, S. *Adv. Funct. Mater.* **2006**, *16*, 2035−2041.
(33) Butler, M. A. *J. Appl. Phys.* **1977**, *48*, 1914−1920.
(34) Saha, R.; Revoju, S.; Hegde, V. I.; Waghmare, U. V.; Sundaresan, A.; Rao, C. N. R. *ChemPhysChem* **2013**, *14*, 2672−2677.
(35) Chaudhari, N. S.; Warule, S. S.; Muduli, S.; Kale, B. B.; Jouen, S.; Lefez, B.; Hannoyer, B.; Ogale, S. B. *Dalton Trans.* **2011**, *40*, 8003−8011.
(36) Xuan, S. H.; Jiang, W. Q.; Gong, X. L.; Hu, Y.; Chen, Z. Y. *J. Phys. Chem. C* **2009**, *113*, 553−560.
(37) Bavykin, D. V.; Parmon, V. N.; Lapkin, A. A.; Walsh, F. C. *J. Mater. Chem.* **2004**, *14*, 3370−3376.
(38) Zhang, D. E.; Zhang, X. J.; Ni, X. M.; Zheng, H. G. *Mater Lett* **2006**, *60*, 1915−1917.
(39) Wu, C.; Xie, Y.; Lei, L.; Hu, S.; OuYang, C. *Adv. Mater.* **2006**, *18*, 1727−1732.
(40) Alivisatos, A. P. *Science* **2000**, *289*, 736−737.
(41) Lou, X. W.; Yuan, C.; Lee, J. Y.; Archer, L. A. *Adv. Mater.* **2006**, *18*, 2325−2329.
(42) Yu, X.; Yu, J.; Cheng, B.; Huang, B. *Chem.—Eur. J.* **2009**, *15*, 6731−6739.
(43) Zhu, L. P.; Liao, G. H.; Bing, N. C.; Wang, L. L.; Xie, H. Y. *J. Solid State Chem.* **2011**, *184*, 2405−2411.
(44) Lei, P. X.; Chen, C. C.; Yang, J.; Ma, W. H.; Zhao, J. C.; Zhang, L. *Environ. Sci. Technol.* **2005**, *39*, 8466−8474.
(45) Zhang, C.; Zhu, Y. *Chem. Mater.* **2005**, *17*, 3537−3545.
(46) Yu, J.; Qi, L. *J. Hazard. Mater.* **2009**, *169*, 221−227.
(47) Xiang, Q.; Yu, J.; Wong, P. K. *J. Colloid Interface Sci.* **2011**, *357*, 163−167.
(48) Hoffmann, M. R.; Martin, S. T.; Choi, W.; Bahnemann, D. W. *Chem. Rev.* **1995**, *95*, 69−96.
(49) Tang, J.; Zou, Z.; Ye, J. *Chem. Mater.* **2004**, *16*, 1644−1649.
(50) Endo, T.; Kobayashi, T.; Sato, T.; Shimada, M. *J. Mater. Sci.* **1990**, *25* (1B), 619−623.
(51) Liu, Z. Y.; Sun, D. D.; Guo, P.; Leckie, J. O. *Chem.—Eur. J.* **2007**, *13*, 1851−1855.